

3D Convolutional Neural Networks for Stalled Brain Capillary Detection

Roman Solovyev¹, Alexandr A. Kalinin^{2,3} , and Tatiana Gabruseva^{4,*}

¹ Institute for Design Problems in Microelectronics of Russian Academy of Sciences, Moscow 124365, Russia; roman.solovyev.zf@gmail.com

² Shenzhen Research Institute of Big Data, Shenzhen 518172, Guangdong, China

³ Department of Computational Medicine and Bioinformatics, University of Michigan, Ann Arbor, MI 48109, USA

⁴ Cork University Hospital, Cork, Ireland; tatigabru@gmail.com

* Correspondence: tatigabru@gmail.com

Abstract: Adequate blood supply is critical for normal brain function. Brain vasculature dysfunctions such as stalled blood flow in cerebral capillaries are associated with cognitive decline and pathogenesis in Alzheimer's disease. Recent advances in imaging technology enabled generation of high-quality 3D images that can be used to visualize stalled blood vessels. However, localization of stalled vessels in 3D images is often required as the first step for downstream analysis, which can be tedious, time-consuming and error-prone, when done manually. Here, we describe a deep learning-based approach for automatic detection of stalled capillaries in brain images based on 3D convolutional neural networks. Our networks employed custom 3D data augmentations and were used weight transfer from pre-trained 2D models for initialization. We used an ensemble of several 3D models to produce the winning submission to the "Clog Loss: Advance Alzheimer's Research with Stall Catchers" machine learning competition that challenged the participants with classifying blood vessels in 3D image stacks as stalled or flowing. In this setting, our approach outperformed other methods and demonstrated state-of-the-art results, achieving 85% Matthews correlation coefficient, 85% sensitivity, and 99.3% specificity. The source code for our solution is made publicly available.

Keywords: Alzheimer's disease; cerebral blood flow; computer vision; deep learning

1. Introduction

Healthy brain vasculature is crucial for maintaining cerebral blood flow (CBF), which supplies neurons with oxygen, energy metabolites, and nutrients. It removes carbon dioxide and other potentially toxic metabolic waste products from the brain and into the systemic circulation for clearance [1,2]. With very limited energy reserve, brain functions stop within seconds if CBF stops, and irreversible damage to neurons occurs within minutes [1,3]. It has been widely acknowledged that disruption of normal CBF is an early and persistent symptom in developing Alzheimer's disease (AD) and other neurodegenerative disorders [1–6]. However, the underlying mechanisms for cerebral blood flow reduction in Alzheimer's disease are not well understood.

Recent advances in imaging technologies, such as multiphoton microscopy, enabled 3D visualization of individual capillaries in living tissue up to about one millimeter in thickness [7,8]. The ability to perform this type of imaging in mouse models of AD offers the opportunity to elucidate the mechanistic links between CBF reductions and AD pathology [6,7]. Typically, the analysis of such images starts with identifying capillaries and then manually labeling each capillary segment as either flowing or stalled based on the motion of blood cells during the entire time each capillary is visible in the three-dimensional image stack [7,9]. However, the process of manual annotation is very tedious and time-consuming, which limits the ability to investigate the vital link between capillary function and AD.

One increasingly popular approach to data annotation that aims to speed up data annotation is crowdsourcing [10], which combines the efforts of many individuals tasked with annotating a small part of a larger data set. This creates an opportunity to use the crowdsourced annotations for training deep



learning models, which rely on the availability of large labeled datasets [11]. Specifically, the growing availability of annotated data has recently enabled efficient applications of deep learning to the analysis of biomedical images [12], demonstrating state-of-the-art results in object detection, segmentation, and classification [13–16]. In multiphoton microscopic images, deep learning have been recently used for segmenting blood vessels [8,17] and segmenting and classifying cancer cells [18–20].

A citizen science project named Stall Catchers (formerly "EyesOnALZ") aims to speed up the identification of stalls in research data using crowdsourcing. To prepare data for annotation by volunteers in Stall Catchers, the raw image stacks of the vasculature are first masked to remove the larger surface vessels and low signal-to-noise regions, and preprocessed to normalize the image intensity distribution and spatial resolution and to remove motion artifacts [21]. After that, capillary regions that need to be annotated are identified using a deep convolutional neural network (CNN) trained to segment cortical blood vessels [21,22]. Finally, the Stall Catchers platform educates and challenges participants with labeling images of individual capillaries as *flowing* or *stalled*. The resulting labeled data have already enabled new scientific studies [21,22], but they also created an opportunity to further improve the data labeling process itself by the application of deep learning.

Here, we propose an approach for the automatic detection of stalled capillaries in 3D brain images from Stall Catchers data using deep convolutional neural networks. To address class imbalance via data augmentation, we also introduce several 3D image augmentation transformations and demonstrate how weights from pre-trained 2D models can be re-used in 3D architectures. Our solution placed 1st out of more than 900 participants of the "Clog Loss: Advance Alzheimer's Research with Stall Catchers" machine learning competition organized by Stall Catchers and DrivenData [23]. Our approach was recognized as the most advanced in both performance and sophistication among competing techniques by the competition organizers, who estimated that our model could automatically analyze about 50% of all existing Stall Catchers data, effectively doubling the analysis speed and helping to uncover insights towards connections between stalled blood flow and AD [24].

2. Materials and Methods

2.1. Problem statement and data description

The dataset used for "Clog Loss: Advance Alzheimer's Research with Stall Catchers" competition was provided by Stall Catchers, a citizen science effort created by the Human Computation Institute [25]. The objective of the challenge was to perform binary classification of the outlined blood vessel segments as either *flowing*, if blood is moving through the vessel, or *stalled*, if the vessel has no blood flow.

Each sample in the dataset contained a set of images (3D image volume) taken from a brain tissue of an alive mouse, showing blood vessels and the blood flow through them. The data had *z* axis in the image volumes, representing both depth—looking at successive layers of brain tissue—and time. See the Stall Catcher's Tutorial [26] for the details. Image volumes were converted to mp4 video files. The dataset contained over 580,000 videos of the blood vessels in brain tissue with a total size of 1.5 terabytes. The target vessel segment for each set of images was annotated with a contour. Figure 1 shown an example of an image from a video set with the annotated vessel.

For each video, the dataset includes metadata that indicates:

- `project-id` – identifier for the research project that generated the video;
- `crowd-score` – crowd-labeled probability that the video is stalled, ranging between 0 (*flowing*) and 1 (*stalled*);
- `tier1` – Boolean variable indicating a highly confident label.

A subset of the videos has been reviewed by an expert, who has labeled videos either *stalled* or *flowing*. Where an expert label is not available, *stalled* vessels are defined as videos with crowd scores greater than or equal to 0.5, while videos with crowd scores less than 0.5 are designated to be *flowing*. The `crowd-score` itself was also provided.

The `tier1` flag column indicates the highest quality data. These are videos that either have an expert-validated label or a highly confident crowd label. A highly confident crowd label was defined

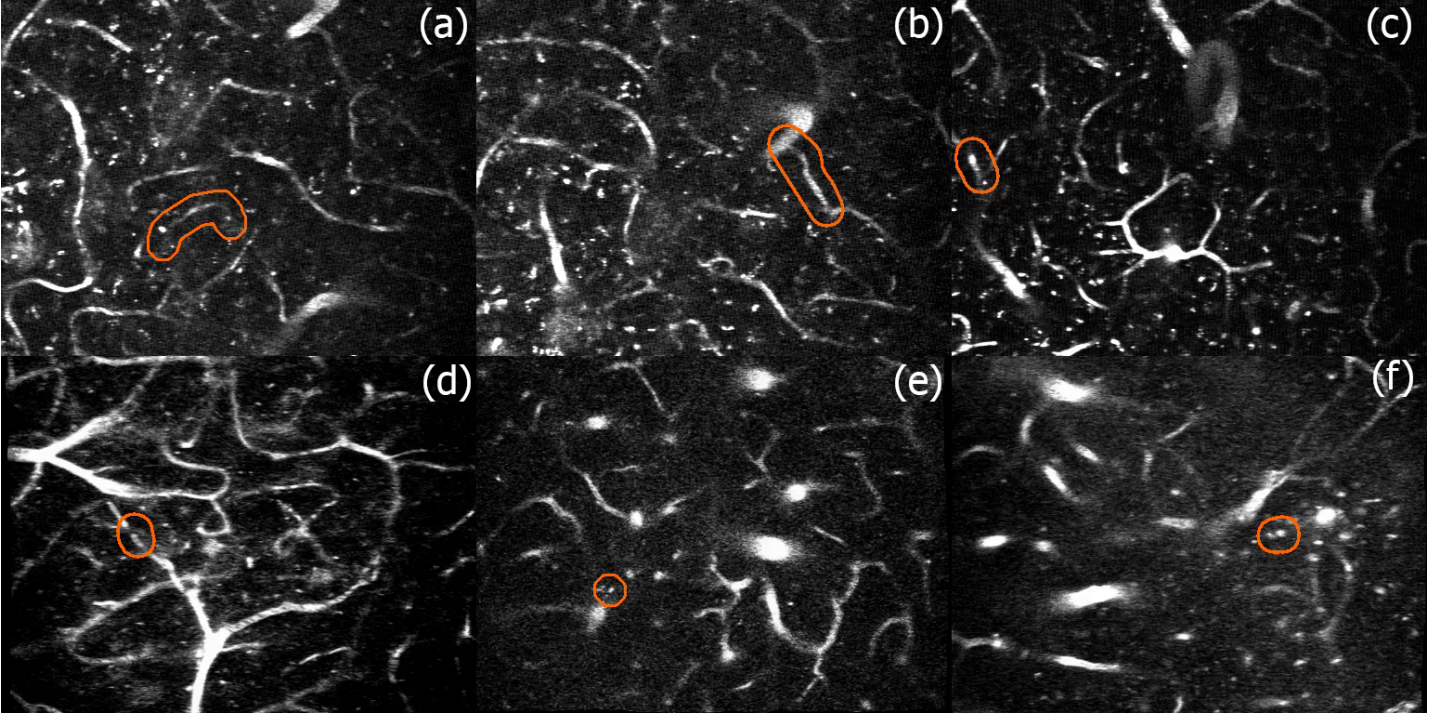


Figure 1. Samples of video frames from mouse brain tissue with the annotated vessel contour (orange) for: (a, b, c) flowing and (d, e, f) stalled vessels.

as one with a crowd score equal to 0 (absolutely flowing) or greater than or equal to 0.75 (most likely stalled). Thus, videos with `tier1` flag can be seen as the most reliable examples of stalled or flowing vessels.

The dataset was highly unbalanced, with 99.7% of videos displaying healthy vessels. There were 1887 videos with stalled vessels, only 706 of them with high confidence (`tier1` flag = 1). The rest, 571161 videos were for the flowing vessels. To help facilitate faster model prototyping, organizers created two subsets of the dataset, referred to as "nano" and "micro", with ratios of stalled to healthy vessels of 50/50 and 70/30, respectively. For our experiments, we used all 1887 videos of stalled vessels, and 50K videos of flowing vessels. To alleviate this class imbalance, we employed heavy data augmentations and undersampling of the *flowing* class as described below. The videos most frequently had 512×384 resolution, with some samples in 418×384 resolution. The distribution of the data in micro train and test sets per format is shown in Table 1.

Table 1: Distribution of video resolution formats in "micro" train and test data sets.

Image set	Resolution	
	512×384	418×384
Train	2380	19
Test	14037	123

The videos had a different number of frames available, between 20 and 300 frames with 60 on average.

2.2. Evaluation

The challenge submissions were evaluated using Matthew's correlation coefficient (MCC), defined as follows [27]:

$$\text{MCC} = \frac{TP \times TN - FP \times FN}{\sqrt{(TP + FP)(TP + FN)(TN + FP)(TN + FN)}} \quad (1)$$

where TP – true positives, FP – false positives, TN – true negatives, and FN – false negatives. This metric takes into account all four components of the confusion matrix and is well-suited for unbalanced datasets.

3. Data preprocessing and augmentations

The region of interest containing the vessel segment (ROI) was annotated in all videos with the orange contour (see Figure 1). We assessed training models both on whole video frames and on cropped ROIs. For the latter, we cropped selected 3D rectangular cuboid around the ROI in all videos. The size of crops with the ROI was usually much smaller than the total video size. Such preprocessing helped to focus models on the relevant data only, as well as optimize training time and computational resources.

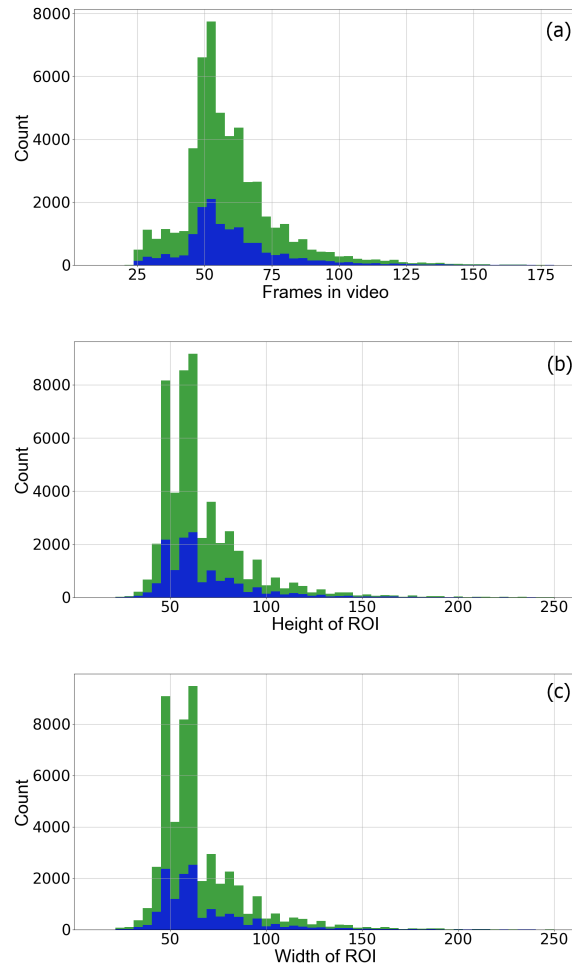


Figure 2. Distribution of ROI sizes for train (green) and test (blue) sets.

Figure 2 shows the distribution of ROI sizes for train and test sets. The average 3D sample size selected was relatively small. The ROIs were around $60 \times 66 \times 67$ pixels, so it was possible to fit several 3D samples into a single GPU memory (NVIDIA 1080Ti, 11 GB). However, all 3D samples had a different sizes.

As the dataset was highly unbalanced, intensive data augmentation was a crucial part of our training pipeline. None of existing data augmentation libraries satisfied our requirements for 3D image data transforms. Therefore, we created a custom library dubbed Volumentations [28], inspired by the open-source library Albumentations [29], that is widely used for 2D images augmentations.

For augmenting 3D samples during training, we used either random mirroring of the 3D image along each of three axes ("mirror 3 axes") or the following complex transformation protocol ("heavy augs"), where p shows the probability of use:

Spatial transformations:

- Random rotation up to 10 degrees along the first axis, $p = 0.3$
- Elastic transform with interpolation, $p = 0.1$
- Rotation by 90 degrees
- Flip along each of the axes, $p = 0.5$
- Grid dropout, $p = 0.1$

Pixel transformations:

- Adding Gaussian noise, $p = 0.2$
- Random Gamma blurring, $p = 0.2$

Custom-made transformations:

- Random crop from borders, $p = 0.4$
- Random drop plane, $p = 0.5$
- Resize, $p = 1.0$

Some of the 3D transforms were adapted from their 2D counterparts implemented in Albumentations [29]: Rotate, ElasticTransform, GridDropout, Flip, RandomRotate90, GaussianNoise, RandomGamma. Other augmentations were developed specifically for this task. For example, RandomCropFromBorders randomly deletes some pixels from one of the 3D sample borders, while RandomDropPlane randomly deletes intermediate 2D planes from some 3D sample axes. The use of Volumentations and "heavy augs" protocol significantly improved the classification performance (see Results).

4. Model architecture

We used 3D CNNs based on Conv3D layers for this classification task. We re-designed commonly-used 2D CNNs architectures, such as ResNet [30], ResNeXt [31], SE-ResNeXt [32], and DenseNet [33], for working with 3D data by replacing all convolutions to Conv3D layers, and changing all other layers respectively, but still keeping the principle architecture and the number of layers as in 2D variant. The architecture of 3D version of DenseNet-121 is shown in Figure 3. This model has a relatively low number of parameters (11.9M), can accommodate the larger batch size, and produced the best classification metrics for this task (see Results).

Backbones pre-trained on Imagenet [34] have demonstrated great results for transfer learning into a different domain with increased accuracy and/or faster convergence [35], including applications to medical image analysis [13–16]. To leverage pre-training on massive 2D image datasets for 3D image analysis, we developed a method for weight transfer from 2D to 3D CNNs. Below, we illustrate the weights transfer on a simple concrete example with a 3D video sample.

For instance, a 3D sample input has following dimensions: (D, H, W, C) , where D , H and W are number of frames, height and width, and C is number of channels. Let's assume $C = 1$ for simplicity (such as in gray scale images), then 3D sample shape is $(D, H, W, 1) = (D, H, W)$. Now, let's take a random frame K (for example, $K = 2$): it will be an image with dimensions $H \times W$. We can compute

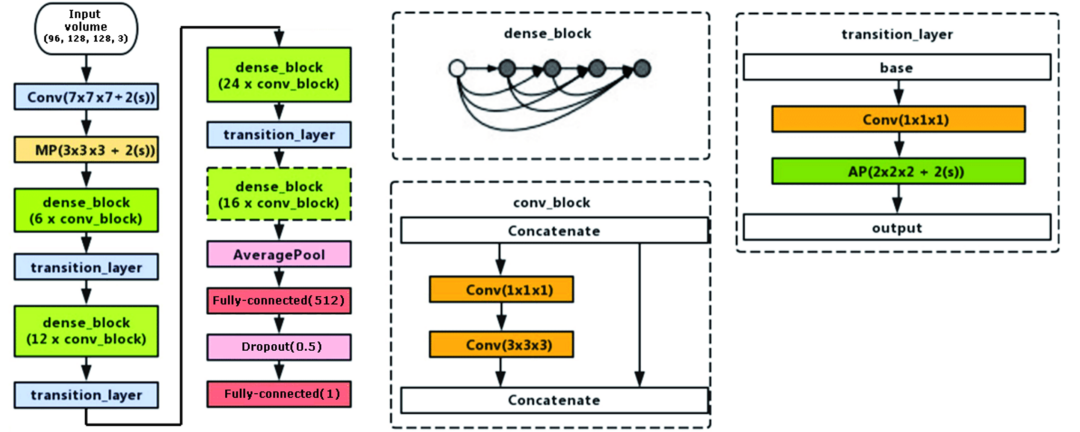


Figure 3. Architecture of DenseNet121 for 3D version. Input dimensions correspond to $frames \times height \times width \times channels$.

feature map for this frame K using $Conv2D$. Let's take a point with i, j coordinates and consider 3×3 region in vicinity of this point, assuming the input frame the following values around this point:

$$F = \begin{pmatrix} 4 & 3 & 2 \\ 1 & -1 & 6 \\ 7 & 1 & 0 \end{pmatrix}$$

If we take a $Conv2D$ convolution with kernel size 3×3 and weights:

$$W = \begin{pmatrix} 2 & 3 & 4 \\ -3 & 0 & 1 \\ 2 & 3 & 6 \end{pmatrix}$$

the output at the feature map for $[i, j]$ point is:

$$Out[i, j] = 2 * 4 + 3 * 3 + 4 * 2 + (-3) * 1 + 0 * (-1) + 1 * 6 + 2 * 7 + 3 * 1 + 6 * 0 = 46 \quad (2)$$

Now, let's consider the 3D volume around the same point in the vicinity $3 \times 3 \times 3$, we take now 3 frames around the point: one frame before and one after previously considered frame. For illustration, we assume they have the following values:

$$F1 = \begin{pmatrix} 3 & 4 & 1 \\ 1 & 0 & 6 \\ 7 & 1 & 0 \end{pmatrix} \quad F2 = \begin{pmatrix} 4 & 3 & 2 \\ 1 & -1 & 6 \\ 7 & 1 & 0 \end{pmatrix} \quad F3 = \begin{pmatrix} 5 & 3 & 2 \\ 1 & 0 & 7 \\ 7 & 2 & 1 \end{pmatrix}$$

We can define a 3D convolution $Conv3D$ with kernel $3 \times 3 \times 3$ in a following way:

$$W1 = \begin{pmatrix} 0 & 0 & 0 \\ 0 & 0 & 0 \\ 0 & 0 & 0 \end{pmatrix} \quad W2 = \begin{pmatrix} 2 & 3 & 4 \\ -3 & 0 & 1 \\ 2 & 3 & 6 \end{pmatrix} \quad W3 = \begin{pmatrix} 0 & 0 & 0 \\ 0 & 0 & 0 \\ 0 & 0 & 0 \end{pmatrix}$$

Here, if we take $W2$ the same as our Conv2D convolution for the second frame, and other parts $W1$ and $W3$ as zero matrices, at 3D point $[2, i, j]$ we will get the same output as in the 2D case:

$$\begin{aligned} \text{Out}[2, i, j] = & 0 * 3 + 0 * 4 + 0 * 1 + 0 * 1 + 0 * 0 + 0 * 6 + 0 * 7 + 0 * 1 + 0 * 0 + \\ & 2 * 4 + 3 * 3 + 4 * 2 + (-3) * 1 + 0 * (-1) + 1 * 6 + 2 * 7 + 3 * 1 + 6 * 0 + \\ & 0 * 5 + 0 * 3 + 0 * 2 + 0 * 1 + 0 * 0 + 0 * 7 + 0 * 7 + 0 * 2 + 0 * 1 = 46 \end{aligned} \quad (3)$$

Applying similar $3 \times 3 \times 3$ kernels to all frames in the input volume, we get a set of feature maps for each frame of the 3D input, in the same manner as if we computed feature maps separately for each frame using Conv2D . Such initialization of weights can be transferred from 2D CNNs pre-trained on ImageNet or other datasets to 3D networks of the same architecture. It provides reasonable initialization as intermediate feature maps contain useful features, even though they are applied to some frames of the video.

Developing this idea further, we can assume that neighbouring frames differ only slightly from each other. Then, we can average feature maps for the close frames. To do that, we create 3D kernel $3 \times 3 \times 3$ with re-distributed weights among the neighbouring frames, as:

$$\begin{aligned} W1 &= \begin{pmatrix} 2/3 & 3/3 & 4/3 \\ -3/3 & 0/3 & 1/3 \\ 2/3 & 3/3 & 6/3 \end{pmatrix} \\ W2 &= \begin{pmatrix} 2/3 & 3/3 & 4/3 \\ -3/3 & 0/3 & 1/3 \\ 2/3 & 3/3 & 6/3 \end{pmatrix} \\ W3 &= \begin{pmatrix} 2/3 & 3/3 & 4/3 \\ -3/3 & 0/3 & 1/3 \\ 2/3 & 3/3 & 6/3 \end{pmatrix} \end{aligned}$$

With such weight re-distribution, we now take into account frames $F1$ and $F2$ while keeping the scale of the values in the output feature map. In this case, the output at point $[2, i, j]$ will be:

$$\begin{aligned} \text{OUT}[2, i, j] = & (2 * 3 + 3 * 4 + 4 * 1 + (-3) * 1 + 0 * 0 + 1 * 6 + 2 * 7 + 3 * 1 + 6 * 0 + \\ & 2 * 4 + 3 * 3 + 4 * 2 + (-3) * 1 + 0 * (-1) + 1 * 6 + 2 * 7 + 3 * 1 + 6 * 0 + \\ & 2 * 5 + 3 * 3 + 4 * 2 + (-3) * 1 + 0 * 0 + 1 * 7 + 2 * 7 + 3 * 2 + 6 * 1) / 3 = (42 + 46 + 57) / 3 = 48.33 \end{aligned} \quad (4)$$

Using this technique, we converted weights from 2D CNNs pre-trained on ImageNet to initialize their 3D counterparts.

5. Model interpretability

Interpretability is an important feature of machine learning models, as it is useful to visualize parts of the samples that CNN is using for classifying. In order to visualize model attention, we used global max pooling instead of average pooling before the classification head. It helps to determine which regions formed feature vectors, as it is determined by the maximum pixel in each feature map. For better clarity of heatmaps, it is critical to use higher input resolution. For instance, for input with $N \times H \times W$ size (N – number of frames, H – height, and W – width), corresponding heatmap size is $N/32 \times H/32 \times W/32$. So, for the input 3D sample with size $128 \times 160 \times 160$ the heatmap size is only $4 \times 5 \times 5$ pixels.

We used inputs with dimensions $320 \times 400 \times 400$ px for creating heatmaps with size $10 \times 13 \times 13$ px. We scaled the heatmap 32 times to match the input resolution and overlaid them with inputs. We

used the last output from the convolution block before the Global Max Pooling layer to plot heatmaps. In our case, feature maps are feature volumes. For 3D ResNet18 it has dimensions of (10, 13, 13, 512), i.e. 512 feature volumes with shapes (10, 13, 13) that transform into a 1D vector of 512 values after 3D global max pooling.

To visualize the heatmaps, we calculated maximum, mean and standard deviation for each point in corresponding (10, 13, 13) volume, as following:

```
# Frames
for i in range(10):
    # Height & width
    for j in range(13):
        for k in range(13):
            heatmap[i, j, k, 0] = out[i, j, k, :].max()
            heatmap[i, j, k, 1] = out[i, j, k, :].mean()
            heatmap[i, j, k, 2] = out[i, j, k, :].std()
```

Using vectorization in numpy [36], these loops can be simplified as:

```
# Layer before pooling
pstd = np.std(out, axis=-1)
pmax = np.max(out, axis=-1)
pmean = np.mean(out, axis=-1)
# Normalize to 0..255 to plot as RGB
nstd = normalize_array(pstd, 0, 255)
nmax = normalize_array(pmax, 0, 255)
nmean = normalize_array(pmean, 0, 255)
# Stack as RGB video
hmap = np.stack((nstd, nmax, nmean), axis=-1)
```

We used maximum, mean, and standard deviation instead of RGB channels. Maximum shows the maximum value possible in this point, standard deviation shows how the weight varies at this point, and mean corresponds to the average influence of this point for the final classification.

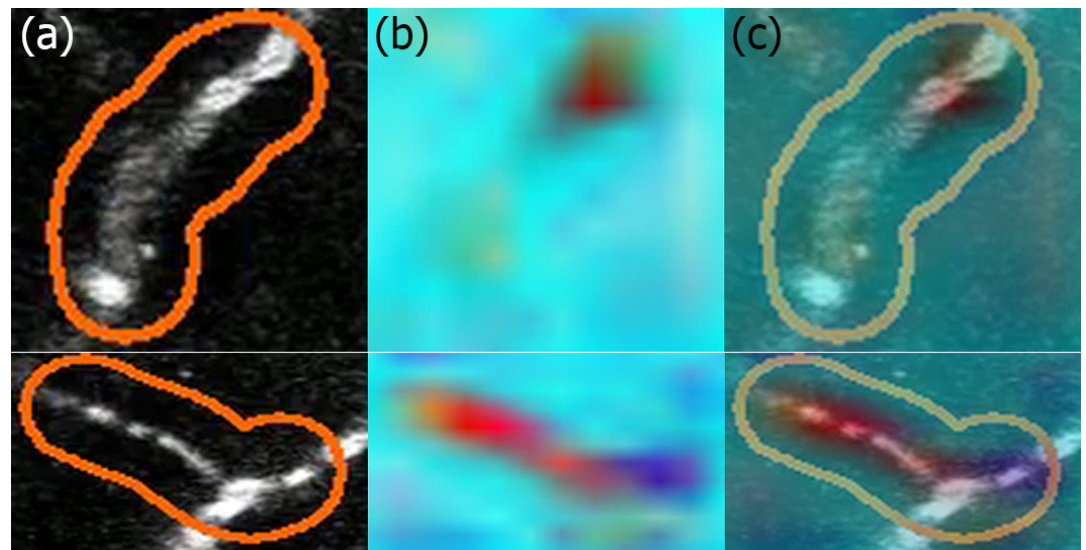


Figure 4. Model attention visualization: (a) input slices cropped around ROI, (b) scaled heatmaps, and (c) overlays of heatmaps with inputs.

6. Results

6.1. Ablation study

First, we illustrated the influence of augmentations on classification performance of the DenseNet121 model. As shown in Table 2, using augmentations led to higher AUC and MCC metrics.

Table 2: Classification metrics achieved with and without augmentations on a validation set.

Model	Input size	Augmentations	AUC	MCC
DenseNet121	(96, 128, 128, 3)	no augs	0.9073	0.5622
DenseNet121	(96, 128, 128, 3)	heavy augs	0.9665	0.7226

We also assessed the utility of 2D-to-3D pre-trained weight conversion for transfer learning. Our experiments showed that weight transfer from 2D model pre-trained on the ImageNet dataset to 3D model robustly helped to decrease convergence time and to improve classification performance results. Specifically, we achieved MCC of 0.810 with DenseNet121 initialized by 2D weight transfer, compared to 0.795 with random initialization. The models with converted weights are available at [37].

6.2. Vessel classification

First, we trained 3D models on the whole video frames rescaled into different sizes, such that they could fit into the 3D model. The results for different input sizes and model backbones are shown in Table 3. The input dimensions of the samples here correspond to $frames \times height \times width \times channels$. Best performance metrics were reached when using larger input resolution of 192×256 , which suggested that small resolution was not enough to capture all important information and motivated us to perform further experiments using ROI cropping to focus on relevant areas in the image, while reducing memory footprint.

Table 3: Results for models trained on videos without ROI cropping.

Model	Input size	Batch size	MCC	AUC	MCC, Test
ResNet18	(64, 96, 128, 3)	20	0.534	0.821	0.4437
ResNet18	(64, 192, 256, 3)	6	0.669	0.892	0.6105
DenseNet121	(64, 96, 128, 3)	10	0.534	0.833	0.4201
ResNet34	(128, 96, 128, 3)	5	0.544	0.840	0.4251
ResNet50	(64, 192, 256, 3)	4	0.697	0.914	0.5986

ROI cropping allowed us to use higher-resolution data, without sacrificing training time and computational resources. On the cropped regions, we tested multiple 3D CNN architectures with different backbones and hyper-parameters, as shown in Table 4. The 3D DenseNet121 demonstrated the overall best classification performance for this task, as measured by both AUC and MCC metrics. This model has a relatively low number of parameters (11.9M), can accommodate the larger batch size, which reduces training time. These results also stress the importance of using heavy augmentations and image sampling to correct for class imbalance.

In order to highlight the areas in the image that influenced network’s decisions, we created model attention heatmaps produced when analyzing stalled capillaries, as shown in Figure 4. These results indicate that the last layer of the 3D CNN is focused on the blood vessel in general, as the shape of the active region in the heatmap overlaps well with the shape of the vessel. Using produced heatmaps we created a video visualization of many analyzed vessels that is available on YouTube [38]. The source code for our solution is publicly available at [39].

7. Discussion

In this paper, we described a solution for automatic brain vessel classification in a highly unbalanced dataset of 3D images. This approach was used to produce a winning solution to the "Clog

Table 4: Results for models trained on cropped ROI regions.

Model	Input size	Parameters	MCC	AUC	MCC, Test
ResNet18	(96, 128, 160, 3)	Mirror 3 axes	0.720	0.927	0.6734
ResNet18	(128, 160, 160, 3)	Heavy augs, Sampler 25%/75%	0.623	0.966	0.7234
DenseNet121	(96, 128, 160, 3)	Mirror 3 axes	0.837	0.959	0.7442
DenseNet121	(96, 128, 128, 3)	Heavy augs	0.641	0.967	0.7887
DenseNet121	(96, 128, 128, 3)	Heavy augs, Sampler 25%/75%	0.649	0.973	0.8129
DenseNet121	(96, 128, 128, 3)	tier1 only, extra-heavy augs, Sampler	0.622	0.958	0.8436
DenseNet169	(64, 128, 128, 3)	Heavy augs			0.7485
DenseNet201	(96, 128, 128, 3)	Heavy augs, Sampler 25% /75%	0.588	0.963	0.7532

Loss: Advance Alzheimer’s Research with Stall Catchers” machine learning competition, which posed a binary classification problem of identifying blood vessels in live mouse brain as *flowing* or *stalled*. Our best solution was based on 3D CNN architecture trained on pre-selected crops with custom 3D image augmentations, balanced sampling, and test-time augmentations. The ablation study has shown the great influence of the data augmentation on the performance of the model. 3D DenseNet121 [40] demonstrated the best performance for this task, achieving MCC of 0.84 and AUC of 0.97 for a single model, which by itself was enough to take first place in the competition. Our final submission to the competition included an ensemble of 18 models with different backbones, demonstrating even further improvement of MCC to 0.855.

The challenge organizers provided outlines for vessels in each video, produced by their segmentation model [8], such that we only had to analyze already pre-selected areas by cropping the ROI around them. To automate the solution even further, one could consider performing simultaneous classification and segmentation of vessels, which could potentially alleviate the requirements of labelling images twice, for localization and for classification. Heatmaps produced by our approach outline vessels of interest well and could be employed as weak labels in the localization/segmentation problem setting.

It is essential to compare the model results with the human labeling approach. Currently, specialized methods aggregate multiple players into a single “crowd answer” that achieves a 0.99 sensitivity and 0.95 specificity threshold on 95% of datasets. Our model gives higher specificity of 0.99 at the cost of lower sensitivity of 0.85. The precision-recall trade-off can be adjusted to fit research and clinical needs by choosing the threshold for binary classification. The results indicate a potential for multiple possible ways of combining machine learning produced annotations and human labeling, which can flexibly address current limitations of data pre-processing and analysis and provide insights towards mechanistic connections between stalled blood flow and AD.

Author Contributions: Methodology, R.S.; software, R.S.; validation, R.S., T.G. and A.A.K.; writing—original draft preparation, R.S., T.G. and A.A.K.; writing—review and editing, R.S., T.G. and A.A.K.; visualization, R.S. All authors have read and agreed to the published version of the manuscript.

Funding: This research received no external funding.

Data Availability Statement: Publicly available datasets were analyzed in this study. These data are made public by the competition hosts in the Amazon S3 bucket named ‘drivendata-competition-clog-loss’.

Acknowledgments: The authors thank the Open Data Science community (ODS.ai) for useful suggestions and other help aiding the development of this work.

Conflicts of Interest: The authors declare no conflict of interest.

Abbreviations

The following abbreviations are used in this manuscript:

AD	Alzheimer's Disease
AUC	Area under the Receiver Operating Characteristic Curve
CBF	Cerebral Blood Flow
CNN	Convolutional Neural Network
GPU	Graphics Processing Unit
MCC	Matthew's correlation coefficient
ROI	Region of Interest

References

1. Zlokovic, B.V. Neurovascular pathways to neurodegeneration in Alzheimer's disease and other disorders. *Nature Reviews Neuroscience* **2011**, *12*, 723–738.
2. Kisler, K.; Nelson, A.R.; Montagne, A.; Zlokovic, B.V. Cerebral blood flow regulation and neurovascular dysfunction in Alzheimer disease. *Nature Reviews Neuroscience* **2017**, *18*, 419.
3. Moskowitz, M.A.; Lo, E.H.; Iadecola, C. The science of stroke: mechanisms in search of treatments. *Neuron* **2010**, *67*, 181–198.
4. Tang, M.; Gao, C.; Goutman, S.A.; Kalinin, A.; Mukherjee, B.; Guan, Y.; Dinov, I.D. Model-based and model-free techniques for amyotrophic lateral sclerosis diagnostic prediction and patient clustering. *Neuroinformatics* **2019**, *17*, 407–421.
5. Sweeney, M.D.; Kisler, K.; Montagne, A.; Toga, A.W.; Zlokovic, B.V. The role of brain vasculature in neurodegenerative disorders. *Nature Neuroscience* **2018**, *21*, 1318–1331.
6. Bracko, O.; Cruz Hernández, J.C.; Park, L.; Nishimura, N.; Schaffer, C.B. Causes and consequences of baseline cerebral blood flow reductions in Alzheimer's disease. *Journal of Cerebral Blood Flow & Metabolism* **2021**, p. 0271678X20982383.
7. Hernández, J.C.C.; Bracko, O.; Kersbergen, C.J.; Muse, V.; Haft-Javaherian, M.; Berg, M.; Park, L.; Vinarsik, L.K.; Ivasyk, I.; Rivera, D.A.; others. Neutrophil adhesion in brain capillaries reduces cortical blood flow and impairs memory function in Alzheimer's disease mouse models. *Nature Neuroscience* **2019**, *22*, 413–420.
8. Haft-Javaherian, M.; Fang, L.; Muse, V.; Schaffer, C.B.; Nishimura, N.; Sabuncu, M.R. Deep convolutional neural networks for segmenting 3D in vivo multiphoton images of vasculature in Alzheimer disease mouse models. *PloS one* **2019**, *14*, e0213539.
9. Bracko, O.; Njiru, B.N.; Swallow, M.; Ali, M.; Haft-Javaherian, M.; Schaffer, C.B. Increasing cerebral blood flow improves cognition into late stages in Alzheimer's disease mice. *Journal of Cerebral Blood Flow & Metabolism* **2020**, *40*, 1441–1452.
10. Michelucci, P.; Dickinson, J.L. The power of crowds. *Science* **2016**, *351*, 32–33.
11. Vaughan, J.W. Making Better Use of the Crowd: How Crowdsourcing Can Advance Machine Learning Research. *Journal of Machine Learning Research* **2018**, *18*, 1–46.
12. Litjens, G.; Kooi, T.; Bejnordi, B.E.; Setio, A.A.A.; Ciompi, F.; Ghafoorian, M.; Van Der Laak, J.A.; Van Ginneken, B.; Sánchez, C.I. A survey on deep learning in medical image analysis. *Medical image analysis* **2017**, *42*, 60–88.
13. Rakhlin, A.; Tiulpin, A.; Shvets, A.A.; Kalinin, A.A.; Iglovikov, V.I.; Nikolenko, S. Breast tumor cellularity assessment using deep neural networks. Proceedings of the IEEE/CVF International Conference on Computer Vision Workshops, 2019, pp. 0–0.
14. Solovyev, R.; Melekhov, I.; Lesonen, T.; Vaattovaara, E.; Tervonen, O.; Tiulpin, A. Bayesian feature pyramid networks for automatic multi-label segmentation of chest X-rays and assessment of cardio-thoracic ratio. International Conference on Advanced Concepts for Intelligent Vision Systems. Springer, 2020, pp. 117–130.
15. Kalinin, A.A.; Iglovikov, V.I.; Rakhlin, A.; Shvets, A.A. Medical image segmentation using deep neural networks with pre-trained encoders. In *Deep Learning Applications*; Springer, 2020; pp. 39–52.
16. Gabruseva, T.; Poplavskiy, D.; Kalinin, A.A. Deep Learning for Automatic Pneumonia Detection. Proceedings of the IEEE/CVF Conference on Computer Vision and Pattern Recognition (CVPR) Workshops, 2020.
17. Haft-Javaherian, M.; Villiger, M.; Schaffer, C.B.; Nishimura, N.; Golland, P.; Bouma, B.E. A topological encoding convolutional neural network for segmentation of 3D multiphoton images of brain vasculature using persistent homology. Proceedings of the IEEE/CVF Conference on Computer Vision and Pattern Recognition Workshops, 2020, pp. 990–991.

18. Lin, H.; Wei, C.; Wang, G.; Chen, H.; Lin, L.; Ni, M.; Chen, J.; Zhuo, S. Automated classification of hepatocellular carcinoma differentiation using multiphoton microscopy and deep learning. *Journal of biophotonics* **2019**, *12*, e201800435.
19. Cai, S.; Tian, Y.; Lui, H.; Zeng, H.; Wu, Y.; Chen, G. Dense-UNet: a novel multiphoton in vivo cellular image segmentation model based on a convolutional neural network. *Quantitative imaging in medicine and surgery* **2020**, *10*, 1275.
20. Huttunen, M.J.; Hristu, R.; Dumitru, A.; Floroiu, I.; Costache, M.; Stanciu, S.G. Multiphoton microscopy of the dermoepidermal junction and automated identification of dysplastic tissues with deep learning. *Biomedical optics express* **2020**, *11*, 186–199.
21. Bracko, O.; Vinarsik, L.K.; Hernández, J.C.C.; Ruiz-Urbe, N.E.; Haft-Javaherian, M.; Falkenhain, K.; Ramanauskaite, E.M.; Ali, M.; Mohapatra, A.; Swallow, M.A.; others. High fat diet worsens Alzheimer's disease-related behavioral abnormalities and neuropathology in APP/PS1 mice, but not by synergistically decreasing cerebral blood flow. *Scientific reports* **2020**, *10*, 1–16.
22. Falkenhain, K.; Ruiz-Urbe, N.E.; Haft-Javaherian, M.; Ali, M.; Catchers, S.; Michelucci, P.E.; Schaffer, C.B.; Bracko, O. A pilot study investigating the effects of voluntary exercise on capillary stalling and cerebral blood flow in the APP/PS1 mouse model of Alzheimer's disease. *PloS one* **2020**, *15*, e0235691.
23. Lipstein, G. Meet the Winners of the Clog Loss Challenge For Alzheimer's Research. <https://www.drivendata.co/blog/clog-loss-alzheimers-winners/>, 2020.
24. Ramanauskaite, E. Stalls, machines and humans: an update. <https://blog.hcinst.org/drivendata-competition-results/>, 2020.
25. Human Computation Institute. <https://humancomputation.org/>.
26. HCI. Stall Catchers introduction and tutorial (August 2018). https://www.youtube.com/watch?v=TjZ4EGTvw_M, 2018.
27. Matthews, B.W. Comparison of the predicted and observed secondary structure of T4 phage lysozyme. *Biochimica et Biophysica Acta (BBA)-Protein Structure* **1975**, *405*, 442–451.
28. Solovyev, R. Volumations 3D. <https://github.com/ZFTurbo/volumations>, 2020.
29. Buslaev, A.; Iglovikov, V.; Khvedchenya, E.; Parinov, A.; Druzhinin, M.; Kalinin, A. Albumentations: Fast and Flexible Image Augmentations. *Information* **2020**, *11*. doi:10.3390/info11020125.
30. He, K.; Zhang, X.; Ren, S.; Sun, J. Deep Residual Learning for Image Recognition, 2015, [arXiv:1512.03385].
31. Xie, S.; Girshick, R.; Dollár, P.; Tu, Z.; He, K. Aggregated residual transformations for deep neural networks. Proceedings of the IEEE conference on computer vision and pattern recognition, 2017, pp. 1492–1500.
32. Hu, J.; Shen, L.; Sun, G. Squeeze-and-Excitation Networks. The IEEE Conference on Computer Vision and Pattern Recognition (CVPR), 2018.
33. Huang, G.; Liu, Z.; Maaten, L.V.D.; Weinberger, K.Q. Densely Connected Convolutional Networks. 2017 IEEE Conference on Computer Vision and Pattern Recognition (CVPR). IEEE, 2017. doi: 10.1109/cvpr.2017.243.
34. Deng, J.; Dong, W.; Socher, R.; Li, L.J.; Li, K.; Fei-Fei, L. ImageNet: A Large-Scale Hierarchical Image Database. CVPR09, 2009.
35. Iglovikov, V.; Seferbekov, S.; Buslaev, A.; Shvets, A. TerausNetV2: Fully Convolutional Network for Instance Segmentation. Proceedings of the IEEE Conference on Computer Vision and Pattern Recognition (CVPR) Workshops, 2018.
36. Harris, C.R.; Millman, K.J.; van der Walt, S.J.; Gommers, R.; Virtanen, P.; Cournapeau, D.; Wieser, E.; Taylor, J.; Berg, S.; Smith, N.J.; Kern, R.; Picus, M.; Hoyer, S.; van Kerkwijk, M.H.; Brett, M.; Haldane, A.; del Río, J.F.; Wiebe, M.; Peterson, P.; Gérard-Marchant, P.; Sheppard, K.; Reddy, T.; Weckesser, W.; Abbasi, H.; Gohlke, C.; Oliphant, T.E. Array programming with NumPy. *Nature* **2020**, *585*, 357–362. doi: 10.1038/s41586-020-2649-2.
37. Solovyev, R. Classification models 3D Zoo. https://github.com/ZFTurbo/classification_models_3D, 2020.
38. Solovyev, R. Alzheimer's Research competition (what neural net sees). <https://www.youtube.com/watch?v=k7s5DCzvKj8>, 2020.
39. Solovyev, R. DrivenData Alzheimer Research 1st place solution. <https://github.com/ZFTurbo/DrivenData-Alzheimer-Research-1st-place-solution>, 2020.
40. Huang, G.; Liu, Z.; Van Der Maaten, L.; Weinberger, K.Q. Densely connected convolutional networks. Proceedings of the IEEE conference on computer vision and pattern recognition, 2017, pp. 4700–4708.